Biosensors and Bioelectronics 190 (2021) 113388

Contents lists available at ScienceDirect

Biosensors and Bioelectronics

journal homepage: www.elsevier.com/locate/bios

A single snapshot multiplex immunoassay platform utilizing dense test lines based on engineered beads

Wonhyung Lee [a,1], Hojin Kim [b,1], Pan Kee Bae [c], Sanghyun Lee [d], Sung Yang [e,f], Joonwon Kim [a,*]

[a] Department of Mechanical Engineering, Pohang University of Science and Technology (POSTECH), Cheongam-ro77, Nam-gu, Pohang-si, Gyeongsangbuk-do, 37673, South Korea
[b] Department of Mechatronics Engineering, Dongseo University, 47 Jurye-ro, Sasang-gu, Busan, 47011, South Korea
[c] BioNano Health Guard Research Center (H-GUARD), 125 Gwahak-ro, Yuseong-gu, Daejeon, 34141, South Korea
[d] Test & System Package, Samsung Electronics, 465 Beonyeong-ro, Seobuk-gu, Cheonan-si, Chungcheongnam-do, 31086, South Korea
[e] Department of Biomedical Science and Engineering, Gwangju Institute of Science and Technology (GIST), 123 Cheomdan-gwagi-ro, Buk-gu, Gwangju, 61005, South Korea
[f] School of Mechanical Engineering, GIST, 123 Cheomdan-gwagi-ro, Buk-gu, Gwangju, 61005, South Korea

ARTICLE INFO

Keywords:
Immunoassay
Rapid test
Microfluidics
COVID-19
Multiplex assay

ABSTRACT

Co-circulation of coronavirus disease 2019 (COVID-19) and dengue fever has been reported. Accurate and timely multiplex diagnosis is required to prevent future pandemics. Here, we developed an innovative microfluidic chip that enables a snapshot multiplex immunoassay for timely on-site response and offers unprecedented multiplexing capability with an operating procedure similar to that of lateral flow assays. An open microchannel assembly of individually engineered microbeads was developed to construct nine high-density test lines, which can be imaged in a 1 mm^2 field-of-view. Thus, simultaneous detection of multiple antibodies would be achievable in a single high-resolution snapshot. Next, we developed a novel pixel intensity-based imaging process to distinguish effective and non-specific fluorescence signals, thereby improving the reliability of this fluorescence-based immunoassay. Finally, the chip specifically identified and classified random combinations of arbovirus (Zika, dengue, and chikungunya viruses) and severe acute respiratory syndrome coronavirus 2 (SARS-CoV-2) antibodies within 30 min. Therefore, we believe that this snapshot multiplex immunoassay chip is a powerful diagnostic tool to control current and future pandemics.

1. Introduction

Human-to-human transmission of infectious diseases commonly occurs by direct or indirect contact (e.g., splash dispersal or mosquito-mediated delivery). Without adequate emergency responses, a local outbreak of a highly contagious disease can turn into a serious global pandemic (van Doremalen et al., 2020; West and Perryman, 2020). Epidemic transmissions are usually controlled and prevented through prompt quarantine actions and the treatment of patients in whom the infection is confirmed after primary clinical diagnosis (Lai et al., 2021; Wang et al., 2020). Therefore, in emergency epidemic situations, accurate and timely diagnosis to distinguish confirmed cases from suspect cases is critical for infectious disease control (Kim et al., 2019; Mohd Hanafiah et al., 2013).

Since late 2019, infection by severe acute respiratory syndrome coronavirus 2 (SARS-CoV-2) has become a severe and unprecedented global pandemic of coronavirus disease 2019 (COVID-19), which continues to be a threat to public health. The World Health Organization's (WHO) official update on April 13, 2021 confirmed that cases and deaths were 136,115,434 and 2,936,916, respectively, in 223 territories (WHO, 2021). To end this pandemic, most governments, laboratories, and businesses are committed to develop and supply new vaccines and diagnostic tools. Reverse transcription polymerase chain reaction (RT-PCR) is the gold standard diagnostic method for this disease, owing to its high accuracy (Corman et al., 2020; Ishige et al., 2020). Unfortunately, the high transmission rate due to the high contagiousness of this infection exceeds the capacity of facilities to perform RT-PCR (Brendish et al., 2020). This expensive laboratory test generally takes several days to provide a result, thus only symptomatic suspects are generally tested. However, it is important to delay viral transmission by quickly isolating

* Corresponding author.
E-mail address: joonwon@postech.ac.kr (J. Kim).
[1] Wonhyung Lee and Hojin Kim contributed equally to the study.

https://doi.org/10.1016/j.bios.2021.113388
Received 13 April 2021; Received in revised form 17 May 2021; Accepted 28 May 2021
Available online 31 May 2021

asymptomatic, pre-symptomatic, and symptomatic patients from public communities (Oran and Topol, 2020). Therefore, massive deployment of rapid and affordable diagnostic tools is critical to handle the required test numbers (Larremore et al., 2020; Oran and Topol, 2020). Indeed, rapid periodic screening could allow societies to re-open much sooner.

Many companies have focused on commercializing portable RT-PCR platforms that offer point-of-care (POC) viral infection testing (Quick et al., 2016; Wang et al., 2020). However, high testing cost, poor scalability, sophisticated pre-treatment procedures, and stringent reagent storage conditions are the bottlenecks for managing large sample numbers (Esbin et al., 2020; Smyrlaki et al., 2020; Wang et al., 2020). Despite the practical shortcomings, molecular diagnostic technology has excellent performance (i.e., accuracy and multiplexing capability); hence, many studies have focused on on-site diagnosis applications (Brendish et al., 2020). After the U.S. Food and Drug Administration (FDA) announced an emergency use authorization (EUA) for SARS-CoV-2 diagnosis, several cost-effective and user-friendly lateral flow assay (LFA)-based antigen tests have been widely distributed (FDA, 2021b; Lai et al., 2021). Though the diagnostic accuracy remains insufficient, public health experts claim that periodic and massive screening could be useful to assess disease prevalence and incidence, regardless of patient symptoms, because symptomatic individuals who test positive represent only a small fraction of all infections (Brendish et al., 2020; Lai et al., 2021; Larremore et al., 2020; Whitman et al., 2020). In September 2020, the FDA announced an EUA for serological COVID-19 IgG/IgM LFA tests, which validated their use to rapidly and easily identify individuals who were recently or previously infected with SARS-CoV-2 (FDA, 2021a). Antibody detection can provide useful data to assess infection and potential immunity within a wide time window and can enable clinical management of SARS-CoV-2 infection (Caruana et al., 2020; Zhao et al., 2020).

Notably, within the peak dengue season, COVID-19 and dengue epidemics overlapped, and cases of co-infection were reported in dengue-epidemic countries (Verduyn et al., 2020). The impact of this co-circulation on public health and patient care remains unclear. Similar clinical manifestations (e.g., fever, cough, and aches) are exhibited in COVID-19 and dengue infection (Lorenz et al., 2020; Verduyn et al., 2020). To make the matter worse, false positives obtained using dengue LFA kits for COVID-19-infected patients in Singapore suggest the possibility of serological cross-reactivity between the two pathogens (Yan et al., 2020). Furthermore, each infection requires a different disease control strategy. When co-circulating pathogens trigger similar clinical manifestations and exhibit serological cross-reactivity, their accurate distinction by multiplexing is the most urgent need in epidemic situations (Balmaseda et al., 2017). However, there are clear limitations to multiplexing (i.e., denaturation, random orientation, and cross-contamination among embedded probes), due to physical adsorption and immobilization of embedded probes in standard LFA kits (Gubala et al., 2012). To overcome such weak multiplexing ability, dual- or triple-testing kits, which parallelize multiple test lines, have been developed (FDA, 2021a). This strategy is technically reasonable to fundamentally prevent crosstalk among each testing line. However, the testing cost and sample/reagent volume are proportionally increased owing to the number of target markers, thus making the kits unaffordable. Thus, despite several efforts, we are still not ready to prevent future pandemics such as the co-circulation of multiple pathogens. Hence, an advanced platform must be established to prevent future pandemics. The platform should achieve the following: (i) multiplexing, (ii) short turnaround time, (iii) affordability, (iv) wide availability, and (v) reliability.

Herein, we propose an advanced platform that enables multiplex one-step immunoassays for timely on-site responses (MOnITOR) with robust and dense test lines based on engineered microbeads. Microbeads were incorporated because of their versatility (i.e., ease of surface functionalization, high stability of conjugates, high surface-to-volume ratio, and mobility), which can allow sensitive multiplex analysis via various encoding techniques (Gilboa et al., 2021; Kim et al., 2017; Lee et al., 2019; Norman et al., 2020; Sankova et al., 2020; Shrivastava et al., 2020). By integrating versatile microbeads, target biomarkers can be easily changed, allowing adoption of this method during the ongoing global pandemic and to prepare for any potential co-epidemic threats and future pandemics (Hemmig et al., 2020). The high-density bead lines can be captured in a single high-resolution snapshot in a narrow field-of-view. Thus, a single snapshot multiplex immunoassay, together with a novel image processing system, could enable reliable and reproducible assessment of fluorescence intensity from the beads. Finally, the MOnITOR chip demonstrated clear multiplexing capability and yielded reliable measurements, thus exhibiting potential as a POC multiplex immunodiagnostic tool.

2. Material and methods

2.1. Reagents and materials

Poly(dimethylsiloxane) (PDMS) Sylgard 184 monomer base and curing agent were purchased from Dow Corning Inc. Photoresist (PR) KMPR 1025 and SU-8 developer were purchased from Microchem, Inc. Blue and red polystyrene beads (~25 μm diameter) were purchased from microParticles GmbH. Carboxylate polystyrene beads (~25 μm diameter) were purchased from Kisker Biotech GmbH. Tween 20, bovine serum albumin (BSA), sucrose, trehalose, sulfo-N-hydroxysuccinimide (sulfo-NHS), 2-(N-morpholino)ethanesulfonic acid (MES; pH 6.0) were purchased from Sigma-Aldrich. 10 mM Tris-HCl buffer (pH 8.0) was purchased from WITHLAB. BSA in phosphate buffered saline (PBS) and 1-ethyl-3-(3-dimethylaminopropyl)carbodiimide (EDC) were purchased from Thermo Fisher. PBS was purchased from Gibco. DyLight 550-labelled anti-mouse IgG polyclonal antibodies (pAb) was purchased from Invitrogen. Recombinant chikungunya virus (CHIKV) E2, Zika virus (ZIKV), and dengue virus (DENV) non-structural protein 1 (NS1) viral proteins, were obtained via baculovirus expression system (provided from BioNano Health Guard Research Center). Anti-ZIKV NS1, anti-DENV NS1, anti-CHIKV E2, and anti-Mayaro virus (MAYV) E2 monoclonal antibodies (mAb) were also provided from BioNano Health Guard Research Center. Recombinant SARS-CoV-2 receptor binding domain (RBD) protein and anti-SARS-CoV-2 RBD mAb were purchased from InvivoGen.

2.2. Fabrication of the microfluidic chip

The top and bottom PDMS substrates of the microfluidic chip were fabricated using a soft lithography technique (Fig. S1) (Xia and Whitesides, 1998). For master mold fabrication, two layers of PR and diced silicon wafer pieces were used. Both PR layers were patterned using KMPR1025, which were dispensed and spin-coated on a cleaned 4-inch silicon wafer (34- and 100-μm thick first and second layers, respectively). Spin-coated wafers were soft-baked at 100 °C, and exposed to ultraviolet light through a photomask. The exposed wafer was post-exposure-baked at 100 °C and developed on an SU-8 developer. This procedure was repeated to pattern the second layer. Finally, two diced wafer pieces [7 × 24 mm and 8 mm (width × length) for the waste reservoir and void, respectively] were bonded to the waste reservoir and vacuum void parts using reflow of the patterned PR hard-baked at 150 °C for 1 min. In general, the areas of microfluidic chip were dominantly increased by the area of the waste reservoir, because the shallow thickness of microchannels fabricated via lithography cannot tolerate waste because of the small microchannel volumes (Olanrewaju et al., 2018). As dummy mold for replica molding, diced wafers thicker than 500 μm can easily provide large volumes for waste and vacuum battery operation, without lithography. The PR-patterned and bare wafers were incorporated to fabricate the top and bottom substrates, respectively. The PDMS monomer base and curing agent were mixed at 10:1 and degassed. The degassed prepolymer solution was poured on master

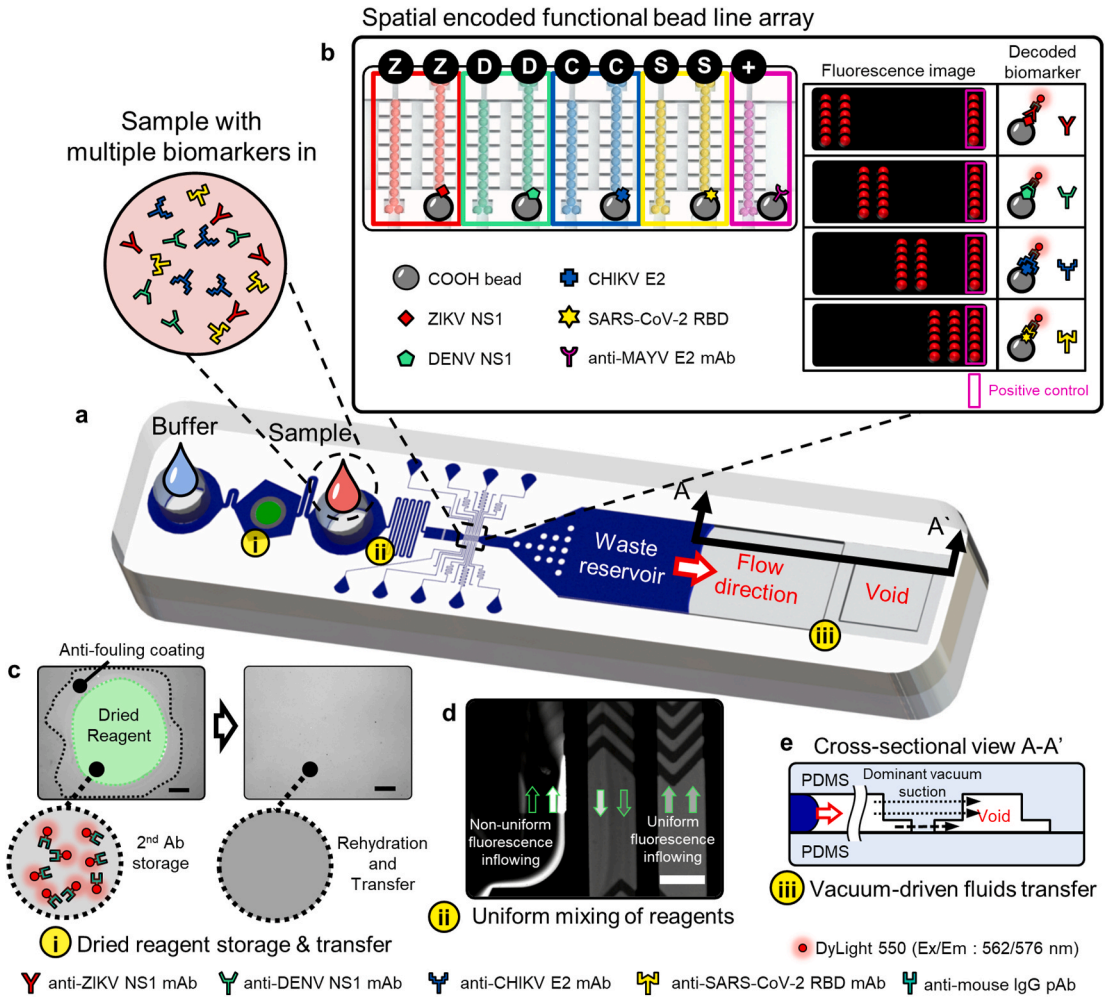

Fig. 1. The MOnITOR chip distinguishes multiple biomarkers. (a) The MOnITOR chip consists of a buffer inlet, sample inlet, reaction zone, and waste reservoir. To conduct a one-step immunoassay, three microfluidic components are integrated: (i) a dried reagent storage and transfer chamber, (ii) a passive micromixer, and (iii) a vacuum-driven fluid transfer void. Loaded buffer and sample with multiple biomarkers flow toward the waste reservoir through the reaction zone. (b) ZIKV, DENV, CHIKV, SARS-CoV-2, and + beads individually form test lines in the reaction zone at their corresponding locations. (c) Dried 2nd Ab is stored in an anti-fouling agent-coated storage chamber (left). The dried reagent is rehydrated by the incoming buffer and is transferred toward the reaction zone (right). Scale bars represent 500 μm. (d) For the indiscriminate reaction within a test line, a staggered herringbone micromixer is incorporated. After passing through a few patterns, non-uniform reagent flow patterns became uniformly mixed. Scale bar represents 200 μm. (e) Cross-sectional view of A-A′, which shows autonomous vacuum-driven fluid transfer by vacuum-incubated nanopores of the PDMS matrix and voids. Using dominant vacuum suction toward the void, continuous fluid transfer can occur for over 30 min.

molds and cured at 100 °C for 20 min. The cured PDMS substrates were detached from the master molds, and the sample and buffer loading inlets were punched with a 4-mm biopsy punch on the top substrate.

On the top substrate, nine high-density bead lines were self-assembled, and the dried reagent was secured. The top substrate was treated with an ambient air plasma (CUTE-MP, FemtoScience) to form the hydrophilic surface property. Using the hydrophilic property, wetting fluid droplets [deionized (DI) water containing 0.5% (v/v) Tween 20 and 0.1% (w/v) BSA] and bead suspension [diluted in 10 mM Tris-HCl buffer] were loaded into the loading ports to form high-density bead lines, as described in the Results section. All bead self-assembly experiments were conducted at a relative humidity of ~20% and room temperature. First, 300 nL anti-fouling coating agent [BSA in PBS containing 5% (w/v) sucrose and trehalose] was loaded in the storage chamber and dried to form a blocking layer where the secondary antibodies (2nd Ab) solution contacted the PDMS surface. Then, 300 nL 2nd Ab solution [250 μg/mL DyLight550-labelled anti-mouse IgG pAb diluted in PBS containing 5% (w/v) sucrose and trehalose] was loaded on the anti-fouling layer and dried. After the bead lines and dried reagent were secured on the top substrate, the bottom substrate was treated with air plasma. Finally, both substrates were irreversibly sealed together. Sealed platforms were incubated at least 1 d for robust bonding and hydrophobic recovery of the PDMS surface.

2.3. Preparation of beads

Carboxylate polystyrene beads (~25 μm diameter) were incorporated and individually engineered to perform the multiplex immunoassay. To tether the probes on beads via covalent bonding, a coupling method using EDC and sulfo-NHS was utilized. Carboxylated beads were incubated and activated in 50 mM MES buffer containing 2-mM EDC and 5 mM sulfo-NHS at room temperature for 15 min. Then, the activated beads were washed three times in 50 mM MES buffer. The activated beads were incubated with recombinant viral proteins or anti-MAYV E2 mAb at room temperature for 2.5 h. Protein-conjugated beads were washed three times in 10 mM Tris-HCl buffer to remove unbound viral proteins. To block non-specific binding, the protein-conjugated beads were incubated in PBS containing 1% (w/v) BSA at room temperature for 30 min. Finally, the protein-conjugated beads were resuspended in 10 mM Tris-HCl buffer at 5×10^5/mL. In every incubation step, the bead

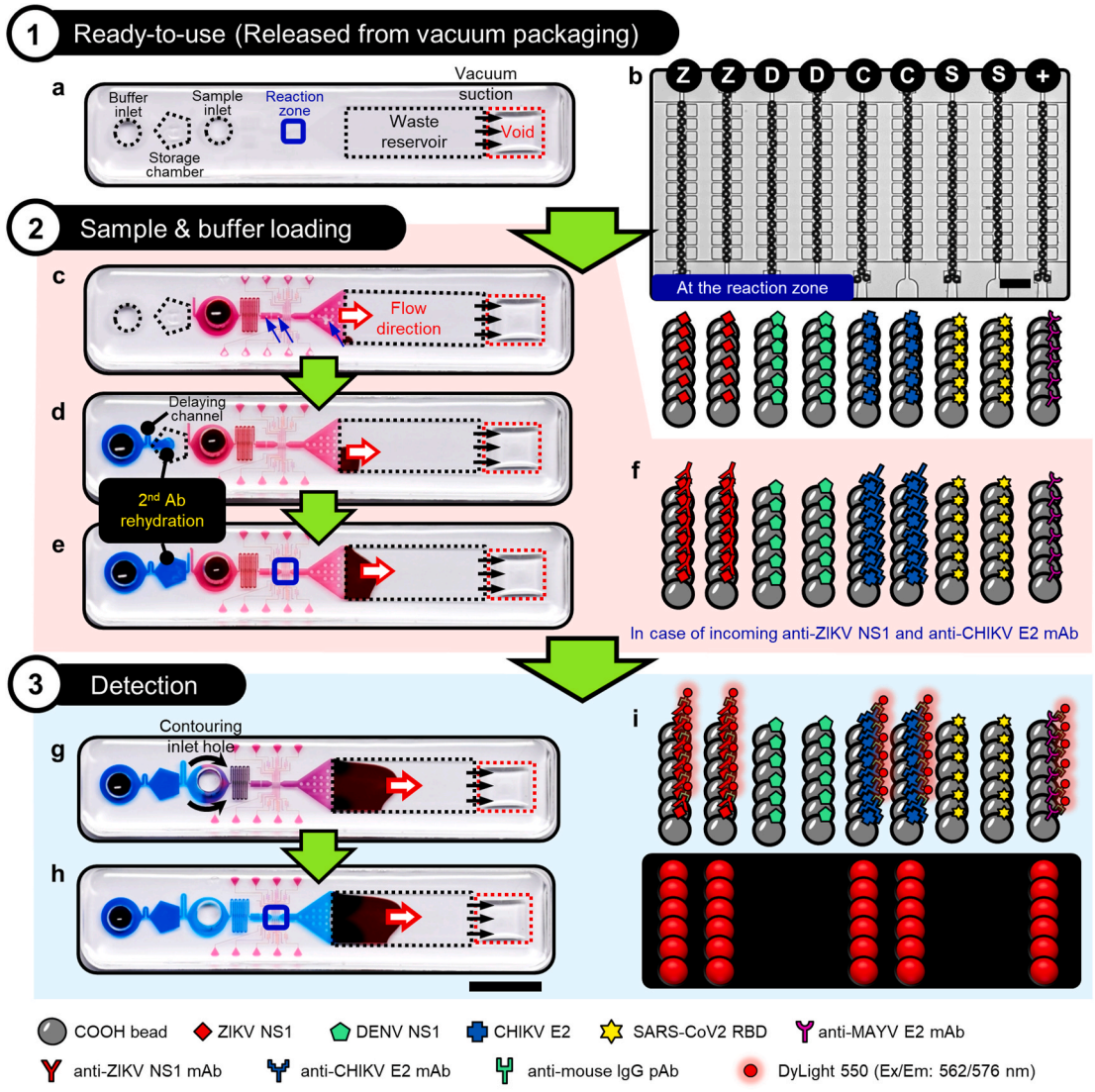

Fig. 2. Operation of the MOnITOR chip for one-step indirect immunoassays. (a) In the 'Preparation' stage, the chip immediately started to operate. (b) Engineered bead lines were secured on the reaction zone. The scale bar represents 100 μm. (c) Red-dyed sample was loaded. Trapped gas bubbles eventually diffused through the PDMS matrix (blue arrows). Wasted volumes in the loading and dummy channels consume only 1.6% of the loaded sample. (d,e) Sequentially-loaded blue-dyed buffer flowed and filled the storage chamber. During storage chamber filling, 2nd Ab was rehydrated. Rehydrated 2nd Ab diffusion toward the buffer inlet was prevented by the delaying channel. (f) When loading sample with anti-ZIKV NS1 and anti-CHIKV E2 mAb, only the corresponding beads reacted. (g) Buffer continuously flowed toward the reaction zone by contouring the empty sample inlet. (h) Unbound 2nd Ab were washed by flowing buffer. An image of the reaction zone was acquired in this stage. The scale bar represents 1 cm. (i) In the case of (f), the transferred 2nd Ab only reacted with ZIKV, CHIKV, and + beads. (For interpretation of the references to color in this figure legend, the reader is referred to the Web version of this article.)

suspensions were shaken by a rotator. For the washing steps, the supernatants were separated from sediment beads by centrifugation at 5000 rpm. (1700 *g*) for 5 min.

2.4. One-step multiplex immunoassay on the MOnITOR chip

The MOnITOR chip consists of the buffer inlet, 2nd Ab storage chamber, sample inlet, passive mixer, reaction zone, waste reservoir, and vacuum battery, sequentially arranged in the flow direction (Fig. 1a). The detailed chip design and dimensions are provided in Fig. S2. The one-step immunoassay can be conducted within 30 min from loading of a sample (40 μL) with multiple biomarkers and of buffer (30 μL) at the corresponding inlets to measure the reaction level on embedded lines, similar to the user-friendly LFA (Fig. 1a). For detecting multiple markers in a single assay, multiple test lines are embedded in a single channel (Fig. 1b). Despite the dense employment, each bead is covalently functionalized with various nanoscaled proteins [i.e., ZIKV, DENV NS1, CHIKV E2, SARS-CoV-2 RBD, and anti-MAYV E2 mAb as a positive control (+)], thereby facilitating multiplexing without cross-contamination among lines. Moreover, the required amount of capture probes, which are generally the most expensive components of immunoassay kits, can be significantly reduced in the MOnITOR chip compared with that in standard LFA kits (Note S1). Therefore, the testing cost was not proportionally increased with the increasing number of target molecules, allowing affordable on-site multiplexing. Once the sample with biomarkers and buffer have been loaded, nine bead lines selectively react with specific antibodies in the sample and fluorophore-labelled pAb as 2nd Ab, in an indirect immunoassay scheme (Fig. 1b). Multiple biomarkers can be identified via a spatial encoding technique using a single fluorophore conjugated to 2nd Ab. To minimize the hands-on time, and eliminate pressure pumping and tube-based sample-to-chip connections commonly used in microfluidic chips, three techniques were incorporated: dried 2nd Ab storage/rehydration/transfer, passive mixing, and vacuum-driven fluid transfer. First, the

storage chamber is coated with an anti-fouling layer to prevent non-specific adsorption of 2nd Ab to the hydrophobic surface. Then, a 2nd Ab solution droplet is deposited and stored in dried-reagent form (Fig. 1c). Once the sample and buffer are introduced, the dried reagent is rehydrated by the buffer and transferred to the reaction zone (Fig. S3) (Gökce et al., 2019; Hemmig et al., 2020). However, due to laminar flow, the transferred 2nd Ab can be discriminately and randomly reacted with beads in each line in the reaction zone. For an indiscriminate reaction across all the beads, regardless of their position, we integrated a staggered herringbone mixer that can passively stretch and fold liquid interfaces, even under a low Reynolds number (Re = ~0.1) (Fig. 1d and S4) (Blicharz et al., 2018; Kwak et al., 2016). Vacuum-driven fluid transport technology in the porous PDMS chips was employed to drive power-free fluid transfer (Dimov et al., 2011). The MOnITOR chip was pre-vacuumed and incubated in a vacuum desiccator. Once the chip was removed from vacuum incubation, the solutions were placed at the inlet ports and suctioned into the chip by vacuum-pressure inside the chip. Pressure build-up occurred at the end of the waste reservoir, which was simultaneously dissipated by gas diffusion through the porous matrix and the vacuum battery, resulting in continuous liquid flow (Yeh et al., 2017). Dominant and continuous gas diffusion occurred through the thin membrane between void and waste reservoir by stored vacuum pressure, which enabled robust liquid transfer over the assay time (~30 min) (Fig. 1e).

2.5. Experimental setup and image analysis

A custom-made vacuum chamber was used to degas the PDMS pre-polymer solution and incubate the MOnITOR chips prior to use under vacuum pressure of −0.95 kPa. All microscopic images and videos were acquired with an inverted microscope (IX 73, Olympus) with a charge coupled device camera (DP 80, Olympus). Fluorescent images were obtained with a light source (SM 365, Lumencor) and filter cube (excitation/emission = 530-550/575–625 nm, U-FGWA, Olympus). A 10 × objective lens (Olympus) was utilized to magnify and acquire all microscopic images. All snapshot images were obtained in TIF format at 1360 × 1024 pixels and a 1.01-μm/pixel resolution with a 14-bit analog for digital conversion.

In general, mean fluorescence intensity (MFI) of reacted beads is calculated in a rectangle region of interest (ROI) on the obtained snapshot. Though the ROI is tightly set along the bead line, noise signals, from background and unintended clogs, are inevitably included in the MFI. Therefore, to subtract noise signal and extract effective pixels from beads in the ROI, pixel intensity-based image analysis was developed and conducted. Detailed schematic and procedure about the image processing are described in section 3.3. ImageJ (National Institutes of Health) was used to set the ROI and obtain the raw data and pixel histogram of fluorescence intensities in the ROI with bins of 2560. Origin software (OriginLab Corporation) was used to obtain the calibration curve of the obtained pixel histogram via multi-peak fitting. Using Excel (Microsoft), effective pixels from the raw data were extracted and MFI of

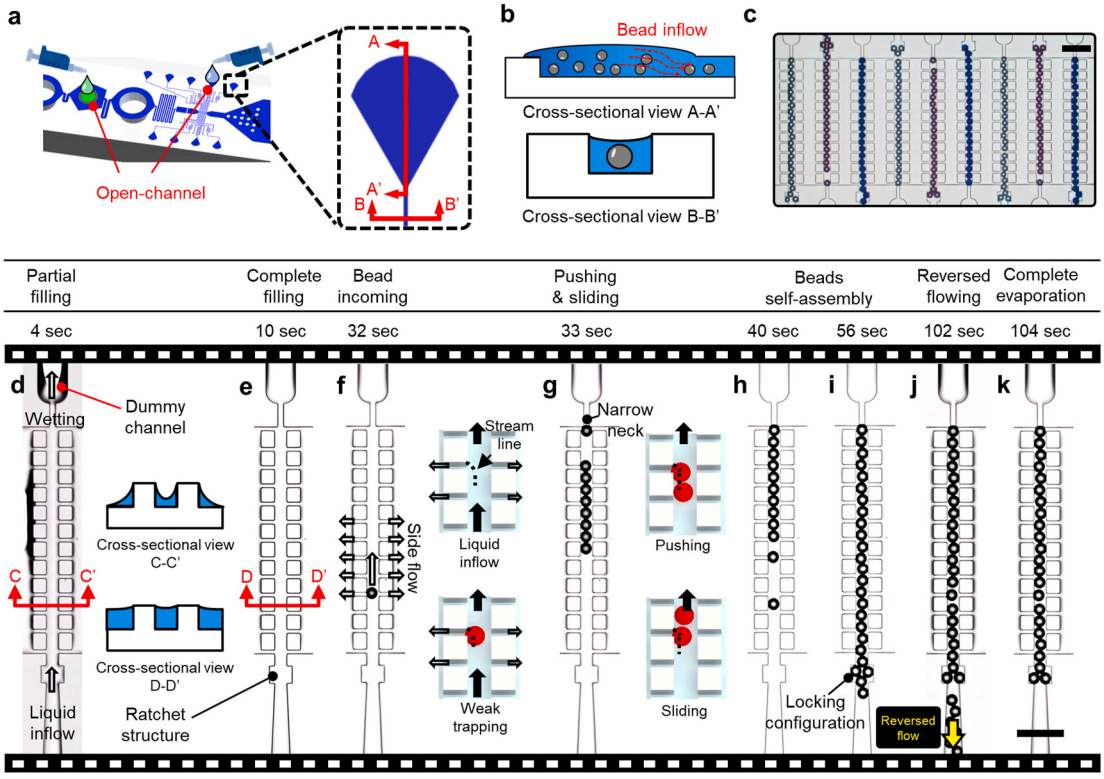

Fig. 3. Mechanism of capillary and evaporation-driven bead line self-assembly. (a) Reagents are added by manual pipetting. The loading ports, which are connected to corresponding locations in the reaction zone, are located outside the main channel. (b) The cross-sectional views represent the introduction of loaded beads into the reaction zone through the microchannel, which is deeper than the bead diameter. (c) Three colored beads (white, red, and blue) were introduced and bead self-assembly was completed in the desired order (white-red-blue sequence). (d) The reaction zone was partially wetted by loading wetting fluids (cross-sectional view of C–C′). Sequentially, the bead suspension was loaded in the connected loading ports. (e) By continuous SCF from the loading ports, the reaction zone was completely filled (cross-sectional view of D-D′). (f) A bead was introduced and weakly trapped in the gap between pillars. (g) The weakly trapped bead was pushed and slid along the pillar array by sequentially introduced beads, until it was completely trapped at the narrow neck of the dummy channel. (h) The weak trapping-pushing-sliding sequence was repeated, and the beads self-assembled and formed a line. (i) The last two beads formed a locking configuration at the ratchet structure. Excessive beads continuously self-assembled. (j) Reversed flow was generated, which removed excessive beads behind the locking configuration. (k) Until complete evaporation, the locking configuration prevented bead loss and sustained the self-assembled bead line. All scale bars represent 100 μm. (For interpretation of the references to color in this figure legend, the reader is referred to the Web version of this article.)

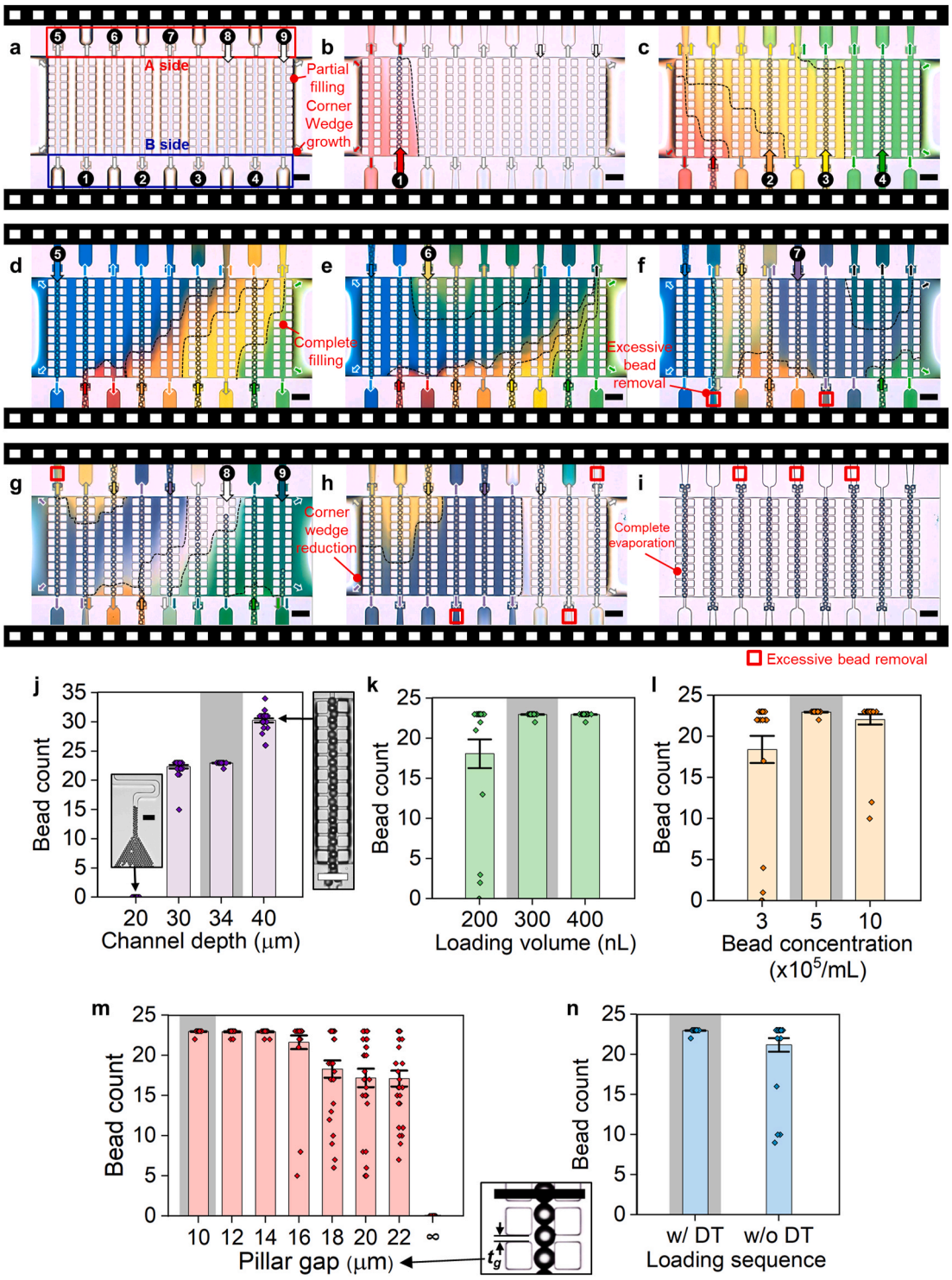

Fig. 4. High-density self-assembled bead line array. (a) From ports #8 and #9, wetting fluids flowed and partially filled the reaction zone by SCF. The A and B sides include ports #5-#9 and #1-#4, respectively. Corner wedges were generated at the boundaries between the main channel and the pillar array. (b) Red-dyed bead suspension (port #1) was applied. Wetting fluid and red dye co-existed, and the boundary is illustrated by the dashed black lines. (c) Orange, yellow, and green-dyed bead suspensions were introduced and generated multiple flow patterns. The wetting fluids were consumed, so non-dyed flow was terminated. (d) After the DT, blue-dyed bead suspensions were loaded in port #5. The dominant hydraulic pressure of the blue-dyed flow biased the other dyed flow patterns. (e) Ivory-dyed flow (port #6) was loaded into the reaction zone. Flow from the B side weakened. (f) Reversed flow was generated from ports #1 and #3. Excessive beads behind the locking configuration were removed (red rectangles). Purple-dyed samples (port #7) were loaded, and other flows were pushed back from the new influx. (g) Non-dyed and turquoise-dyed bead suspensions (ports #8 and #9, respectively) were loaded. Reversed flow was generated from port #5. (h) The corner wedges were reduced because there was no more medium supply. Excessive beads at ports #2, #4, and #9, were removed. (i) Finally, a droplet of wetting fluid was loaded next to the reaction zone to washing out excessive beads in ports #7-#9. After complete evaporation, a high-density self-assembled bead line array was successfully constructed in the reaction zone. (j–n) Effects of channel depth, loading droplet volume, bead concentrations, pillar gaps, and DT on bead self-assembly. The grayed areas represent the optimized conditions for each parameter. Data represent the mean ± standard error of the mean (s.e.m.) of the number of self-assembled beads (n = 25). All scale bars represent 100 μm. (For interpretation of the references to color in this figure legend, the reader is referred to the Web version of this article.)

the effective pixels was calculated. All MFIs of bead lines were obtained via this image processing technique.

2.6. Determination of a threshold value for qualitative detection

A threshold value was determined to differentiate the test results. The device was prepared as shown in Fig. 1 and blank samples (0 ng/mL in PBS) were tested. MFIs of effective pixels from 8 bead test lines, except for the positive control lines, were extracted and measured via image processing in all snapshots from each assay. A threshold value was set as the mean + 3 standard deviation (s.d.) (877.184) of values from blank sample assays (n = 128; 16 snapshots with 8 lines each).

3. Results and discussion

3.1. Operation of the MOnITOR chip

Operation of the MOnITOR chip proceeded autonomously in three stages: 1) preparation, 2) sample and buffer loading, and 3) detection. At the 'Preparation' stage, the chip with non-reacted bead lines, started to imbibe air itself by pressure difference (Fig. 2a and b). When we loaded the chip with red dye, it filled the microchannels within 1 min and flowed toward the reaction zone and waste reservoir (Fig. 2c). Rapid and effective degassing from the microchannel provided reproducibility of the designed flow. As the sample type varies depending on the sample origin and target molecule to be diagnosed, inter-assay variation may significantly increase if the dried 2nd Ab reagent is rehydrated by the sample. To inhibit sample inflow to the dried reagent, the microchannel between the buffer inlet and the storage chamber was designed to be deeper than other channels (100- vs 34-μm deep, respectively). Sample flow stopped at the depth boundary, which worked as a capillary stop valve (Fig. S5) (Glière and Delattre, 2006). Additionally, subsequently loaded buffer could only flow into the deeper channel by a burst of lower pressure to reliably rehydrate the dried reagent (Fig. 2d and e). The sample and buffer solution flowed sequentially driven by the vacuum battery and waste reservoir. Upon loading samples with anti-ZIKV NS1 and anti-CHIKV E2 mAb, these mAbs specifically reacted with ZIKV and CHIKV beads (Fig. 2f). Loaded sample was continuously transferred to the waste reservoir and completely consumed. Then, the buffer with rehydrated 2nd Ab was introduced through contouring channels around the sample inlet port (Fig. 2g). The contouring channel plays a crucial role in sustaining continuous buffer flow. These channels sustained the air-liquid interface around the sample inlet port by balancing negative Laplace pressure and hydraulic pressure, preventing undesired inflow of air bubbles (Fig. S6). At the reaction zone, the introduced 2nd Ab selectively reacted with target biomarker-captured and + beads. Unbound 2nd Ab were washed by introducing fresh buffer without 2nd Ab (Fig. 2h). A snapshot of the bead line was then acquired. Only ZIKV, CHIKV, and + beads reacted with the 2nd Ab; thus, biomarkers in the sample were identified based on the line position with a single wavelength fluorescence signal (Fig. 2i). Using this operating scheme, indirect immunoassays take ~30 min from sample and buffer loading without any additional actions. The anti-ZIKV NS1 mAb was selected as a representative and detected to validate the immunoassay scheme itself performed well. Also, the antigen-antibody binding performance of the microfluidic platform in continuous flow conditions was evaluated by comparing the immunoassay protocol in vials, which has incubation steps for sufficient reaction (Acharya et al., 2016). The limit of detection (LOD) for anti-ZIKV NS1 mAb detection was 3.0- and 1.2 ng/mL for the microfluidic and vial assays, respectively. Although there is no incubation step in the one-step immunoassay in the MOnITOR chip, the calculated LOD was similar to that of the vial assays. These results indicate rapid, yet sensitive immunoassays were possible by utilizing continuous flow, short diffusion length, and the high surface-to-volume ratio of the microfluidic nature (Kim and Herr, 2013). Fig. S7 provides details of the immunoassay protocol.

3.2. Open channel self-assembly of bead test lines

A novel open microfluidic-assisted bead self-assembly technique was developed to construct dense lines that cannot be achieved via current direct printing technology. Multiple microfluidic channels with loading ports, which are large enough to directly load each bead droplet, were physically connected to the compact bead lines in the reaction zone (Fig. 3a). The multiple bead lines were then produced by capillary and evaporation-driven bead flow in an open channel environment (Choi et al., 2010; Hemmig et al., 2020). Liquid flow compensated for evaporation on the upper surface of the liquid channel and allowed beads to move until the bead suspension in the port dried.

At the reaction zone, a sophisticated channel composed of two micropillar lines and a ratchet structure was designed to allow unblocked bead inflow and prevent the escape of trapped beads. Various bead types can be easily loaded by manual pipetting. Spontaneous capillary flow (SCF) and evaporation through the entire open microchannels conveyed the loaded beads to the reaction zone via connected microchannels, which were designed to be deeper (~34 μm) than the bead diameter (~25 μm) (Fig. 3b). Thus, the engineered beads can independently assemble themselves in the desired order without cross-contamination between bead types (Fig. 3c).

To understand the bead self-assembly mechanism, a single bead line was constructed. Droplets of wetting fluid, which were used to prefill the microchannel and block non-specific surface binding, were loaded prior to loading the bead suspensions (Fig. 3d). Once the microchannels were partially filled by SCF, a droplet of bead suspension was loaded (Fig. 3e). A dummy channel and a side channel were added to enhance evaporative flow and to allow main channel flow, respectively. After the gaps between the pillar array were completely filled by continuous SCF from the loading ports, beads were introduced by sideways flow and flow through the dummy channel (Fig. 3f). Flow fractionation occurred by vertical flow, and the introduced bead was weakly trapped between pillars (~10-μm gap), which were designed to be smaller than the bead diameter. During continuous SCF, the weakly trapped bead was pushed along the pillar array by sequentially introduced beads. The weak trapping-pushing-sliding sequence was repeated until the beads were completely trapped at the narrow neck of the dummy channel and the channel was filled with pre-assembled beads (Fig. 3g and h). Once the line was fully occupied, the last two beads formed a locking configuration in the ratchet structure (Fig. 3i). The superior monodispersity of beads and the reproducible structures based on replica molding played a crucial role to repeatedly make the locking configuration. During self-assembly, the droplet volume in the loading port was continually reduced by spontaneous evaporation and consumption by SCF. When the droplet was almost consumed, thin wedges at the edge of the loading port formed, which generated capillary pressure and continuous evaporation (Fig. S8). Therefore, the flow direction was quickly reversed toward the loading port, which removed excessive beads behind the locking configuration (Fig. 3j). In total, 23 beads formed a bead line under fluidic oscillation until the self-assembly was completed (Fig. 3k).

Using single-line self-assembly, high-density bead lines can be consistently constructed. Each loading port was numbered from #1 to #9 and the droplet loading sequence was fixed as W#8-W#9-B#1-B#2-B#3-B#4-B#5-B#6-B#7-B#8-B#9 to increase bead inflow to the reaction zone ('W' and 'B' stand for wetting fluid and bead suspension loading, respectively) (Fig. 4a and Fig. S9). We analyzed this sequence to simplify the complex fluidic correlation in the multiple open channel environment and ensure consistent bead self-assembly (Fig. 4a–i). To visualize the stream lines, 9 different colored fluids were used as bead suspension media. Before loading the bead suspensions, droplets of non-dyed wetting fluid were loaded in ports #8 and #9 (Fig. 4a). The pillar array and microchannel were partially filled by SCF, and corner wedges on the boundaries between the pillar array and wide channels were grown by continuous SCF of the wetting fluid. Droplets of dyed bead suspension were loaded in ports #1-#4. The flows from the A and B sides

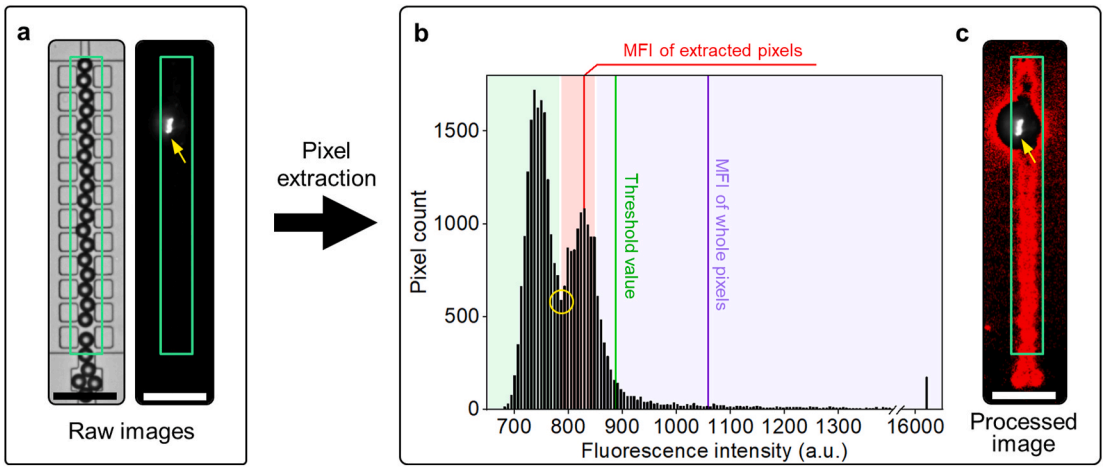

Fig. 5. Pixel intensity-based image analysis to extract effective pixels and subtract noise. (a) Raw images [bright field (left) and fluorescence (right)] of a bead line were acquired 30 min after loading blank sample and buffer. The green rectangles represent the bead line ROI. Any biomolecules that were not loaded, but 2nd Ab aggregates, which produce signal noise were clogged the bead line (yellow arrow). (b) Pixel histogram of fluorescence intensities acquired from the bead line ROI. Including the clogs, the MFI of all pixels (violet line) exceeds the threshold value (green line), which results in false positive results. A valley point (yellow circle) was selected between the two peaks. Pixels with signals lower than the valley point were subtracted as background signals. From the valley point to the upper 90% point (red and violet area), pixels with the 10 most frequent intensities were picked (red area). In this area, the calculated MFI (red line) is lower than the threshold value, which results in a true negative result. (c) Applying the values from the red area in (b) to the fluorescence image in a highlights the effective pixels (red color), which cover most of the beads. All scale bars represent 100 μm. (For interpretation of the references to color in this figure legend, the reader is referred to the Web version of this article.)

coexisted and mixed by diffusion during laminar flow (Fig. 4b). From the B side, various colored flows were introduced, which generated multiple laminar flow patterns and moved out through nearby or opposite dummy and side channels (Fig. 4c). Then, a 30 s delaying time (DT) after loading port #4 was used before loading the bead suspension in ports #5-#9. DT can delay and shorten the capillary saturation, which can cause potential bead self-assembly failure (Fig. S10). Once the droplets were loaded in ports #5-#9, media from the loading ports were maximized and caused complete filling in the pillar array (Fig. 4d). At this stage, the droplets at the B side were almost consumed, so the flow boundaries were biased (Fig. 4e). After the droplets in each port were nearly consumed, reversed flows were generated to remove excessive beads behind the corresponding locking configurations (Fig. 4f–i). Because there was no additional media loading, the corner wedges started to reduce (Fig. 4h). After complete evaporation, high-density self-assembled bead lines were successfully constructed (Fig. 4i and Video S1).

Supplementary video related to this article can be found at https://doi.org/10.1016/j.bios.2021.113388

Each bead line was designed to contain 23 beads in a single row in the same snapshot focal plane, which allows reliable measurement. Testing lines composed of multi-layered beads limited the reproducible setting of a focal plane. As the focal plane was changed, intra- and inter-assay variance of the multiplex immunoassay was significantly increased. Parametric tests were conducted to optimize the conditions that can consistently construct lines with 23 beads after complete evaporation. The effect of channel depth, droplet loading volume, bead concentration, pillar array gaps, and DT on the self-assembly of 23 beads, were characterized. Optimized conditions of all parameters are represented by gray background on the corresponding graphs (Fig. 4j-n). Four chips with various microchannel depths (i.e., 20-, 30-, 34-, and 40-μm) and a 10-μm pillar gap were tested (Fig. 4j). As the microchannel depth increased, SCF was enhanced and the likelihood of bead inflow was increased (Ryu et al., 2008). In the chip with 20-μm deep microchannels, the bead diameter was larger than the channel depth. The beads were partially immersed, which causes the surface tension force between beads and air-liquid interface to dominate other forces (Fig. S11). Under these conditions, all beads clogged at the droplet boundary in the loading port and could not flow into the reaction zone (Fig. 4j, left). In the chip with 30-μm microchannels, though the microchannel was deeper than the bead diameter, the filling height of the medium in the microchannel varied depending on the status of media supply. In a partially filled state, the upper meniscus profile was smaller than bead diameter, which inhibited bead inflow and resulted in a failure to form the locking configuration. In contrast, the 40-μm deep chip offered strong SCF, which enhanced bead inflow toward the reaction zone. However, the self-assembled beads formed a Miller index (110)-like configuration with a channel depth/bead diameter ratio of 1.5 (Fig. 4j, right) (Hatch et al., 2011). The 34-μm deep chip provided the most reliable self-assembly with 23 beads in a single layer.

Fig. 4k demonstrates the effect of loading volume on bead self-assembly (bead concentration = 5×10^5/mL). By loading 200 nL droplets, the media and bead supply was insufficient to form the locking configuration. Using 300-nL droplets, repeatable self-assembly was achieved. However, 400 nL droplets caused droplet merging in the loading ports. Therefore, 300 nL droplets was loaded for all characterization tests. At 3×10^5/mL, the locking configuration was irregularly formed by a lack of bead inflow (Fig. 4l). However, channel clogging sometimes occurred at 10×10^5/mL. Thus, 5×10^5/mL was selected as the optimized bead concentration.

To reliably repeat the weak trapping-pushing-sliding bead sequence, various gaps (t_g) in the pillar array (10-, 12-, 14-, 16-, 18-, 20-, and 22-μm gaps, and no pillar conditions) were tested (Fig. 4m). As the gap became wider, the beads were more strongly trapped. Thus, the weak trapping-pushing-sliding sequence was not reliably repeated in chips with >16-μm gaps. For 12- and 14-μm gap chips, repeatable self-assembly was achieved, but the 10-μm gap chip was chosen to allow weaker bead trapping. For no pillar chips, incoming of beads was prevented. Chips with a narrower gap were not fabricated or tested for reproducible fabrication. The DT was also tested, and repeatable self-assembly was achieved with a 30-s DT (Fig. 4n). The optimal conditions for all parameters were utilized to fabricate chips for all subsequent experiments. After the bead lines were constructed, the PDMS layer was permanently bonded to a plasma-treated flat PDMS layer. Finally, the chip was incubated under vacuum to be the 'Preparation' stage.

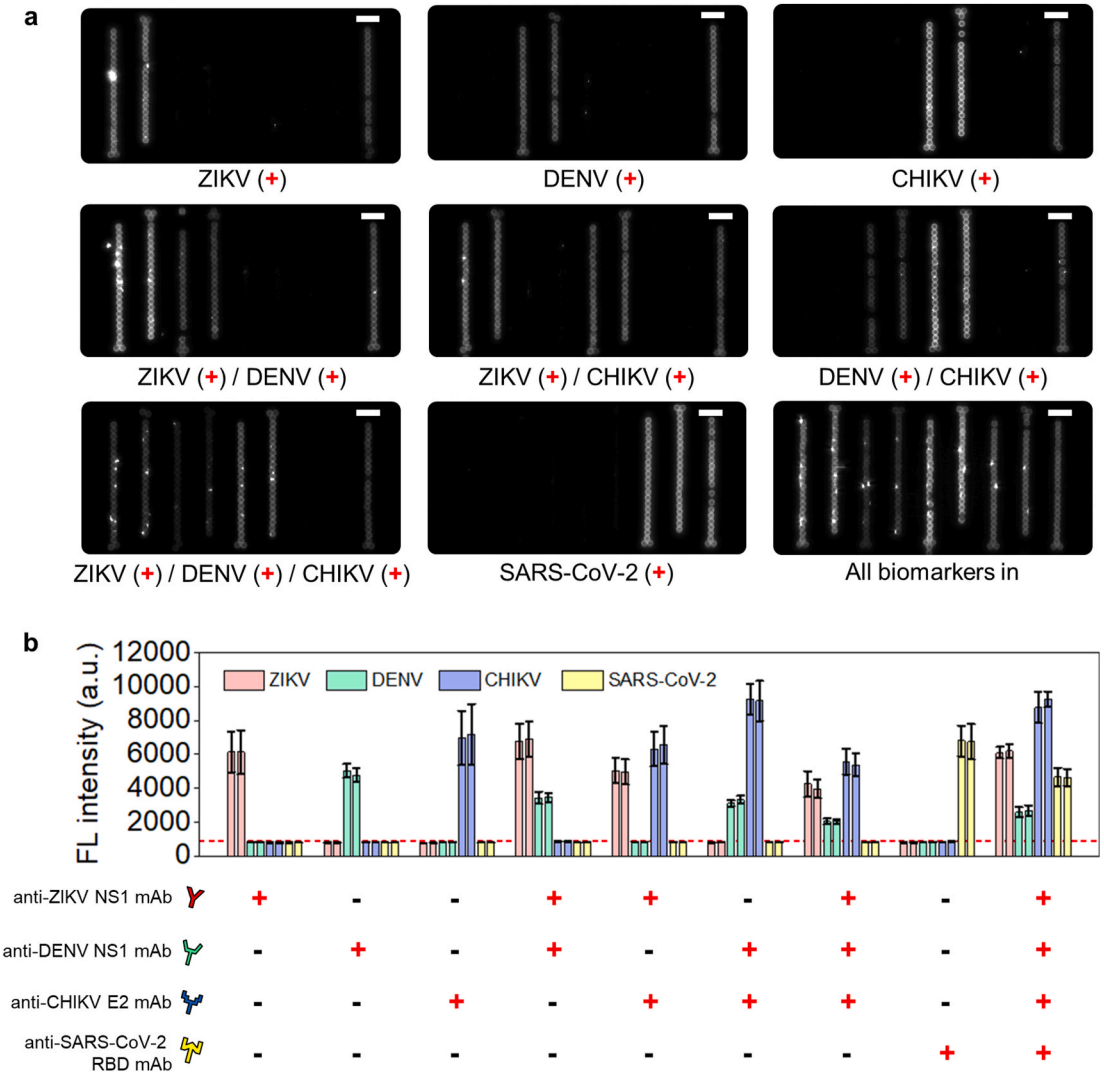

Fig. 6. Fluorescence-based multiplex detection of biomarkers via spatial encoding. (a) Fluorescence images acquired after one-step multiplex immunoassay. Various biomarker combinations (anti-ZIKV NS1, anti-DENV NS1, anti-CHIKV E2, anti-ZIKV/DENV NS1, anti-ZIKV/CHIKV NS1/E2, anti-DENV/CHIKV NS1/E2, anti-ZIKV/DENV/CHIKV NS1/E2, anti-SARS-CoV-2 RBD, and all biomarkers) were spiked and tested as possible scenarios in co-circulating disease situations. Only the corresponding beads were illuminated. (b) Fluorescence (FL) intensities from each bead line with various biomarker combinations. The signals were obtained using pixel intensity-based image analysis. Only the corresponding bead lines emitted fluorescence intensities that exceeded the threshold value (dashed red line). Data represents the mean ± s.d. of fluorescence signals from assays in triplicate. All scale bars represent 100 μm. (For interpretation of the references to color in this figure legend, the reader is referred to the Web version of this article.)

3.3. Fluorescence intensity-based extraction of effective pixels

The level of multiple reactions can be measured by analyzing a single image of the reaction zone. A rectangular ROI was tightly set along the bead line to minimize background signals (Fig. 5a). By measuring the fluorescence intensity inside the ROI, immunoreaction level can be evaluated. However, 2nd Ab aggregates, clogs, and non-targeted molecules can flow in, which might clog narrow gaps and adsorb onto the bead and substrate surface, causing signal noise and false positive results. To address these challenges, a novel image processing method was developed to extract effective pixels from beads and subtract signal noise. Even in a test with no biomolecules, clogs flowed in and caused severe noise in the ROI (Fig. 5a). In Fig. 5b, a pixel histogram corresponding to fluorescence intensity inside the ROI is presented. Clogs in the ROI manifested as pixels with saturated intensity (16,383). Although these pixels are only a small fraction of all pixels in the ROI (0.55%), their intensity was strong. Therefore, as shown in Fig. 5b, simply calculating the MFI of all pixels as the final value resulted in a false positive result greater than the threshold value.

The fluorescence histogram of the ROI has two fluorescence peaks from the bare and bead-populated portions (Fig. 5b). With multi-peak fitting, a valley point (yellow circle) can be measured and background signals from the bare portions (green area) can be separated and subtracted (Fig. 5b and Fig. S12). As clogs generally cause saturated fluorescence intensity, pixels with fluorescence intensity in the upper 90% or higher were subtracted. In the range from the valley to the upper 90% (red and violet areas), pixels with the top 10 most frequent intensities were extracted (Fig. 5b); the effective pixels cover most of the bead portions (Fig. 5c). Signals caused by clogs and partially covered beads contribute to the overall signal, but the bead line was designed to be occupied by 23 beads, rather than a single bead. Thus, the value is predominantly derived from the bead line, and the extracted pixels can represent the effective signal from beads. The MFI of the extracted pixels was recognized as the final assay value (Fig. 5b). Using this approach, high immunoassay specificity was achieved. The MFI in all images in this study was measured in this manner.

3.4. A single snapshot multiplex immunoassay

As shown in Fig. 1b, the test lines were arranged in the order of ZIKV, ZIKV, DENV, DENV, CHIKV, CHIKV, SARS-CoV-2, SARS-CoV-2 and + beads on the reaction zone. To test the current disease state and a possible scenario of overlapped outbreaks, a multiplexed combination of arboviruses and COVID-19 was used. The WHO recommends multiplexing ZIKV, DENV, and CHIKV as an ideal detection method, and this combination was found to allow virus distinction in possible co-circulation situations (do Rosario and de Siqueira, 2020; WHO, 2016). Qualitative multiplex immunoassays using a threshold value to define positive or negative results were demonstrated with randomly spiked samples in PBS (i.e., anti-ZIKV NS1, anti-DENV NS1, anti-CHIKV E2, anti-ZIKV/DENV NS1, anti-ZIKV/CHIKV NS1/E2, anti-DENV/CHIKV NS1/E2, anti-ZIKV/DENV/CHIKV NS1/E2, anti-SARS-CoV-2 RBD, and all biomarkers). The concentration of each antibody in all samples were all 2 μg/mL, which is a higher concentration than used in the LOD calculation (Fig. S7). This is for easily and visually showing the conceptualization of the MOnITOR chip. With each loaded spiked sample, only the corresponding bead lines were clearly illuminated (Fig. 6a). The effective pixels were detected within each line using pixel intensity-based image analysis. Although 2nd Ab aggregates and clogs led to the appearance of unintended signals at bead lines, the intra-assay variation between two lines with same capture probes (i.e., 1st and 2nd ZIKV lines, 3rd and 4th DENV lines, 5th and 6th CHIKV lines, and 7th and 8th SARS-CoV-2 lines) was significantly reduced by image processing, improving the reliability of measurements (Fig. 6a and b). The final values from the corresponding bead lines exceeded the threshold value, while the others did not (Fig. 6b). These results validated the use of single snapshot multiplex immunoassays for simultaneous detection of four different biomarkers. However, inter-assay variation among sample mixtures (e.g., anti-DENV NS1 vs anti-ZIKV/DENV/CHIKV NS1/E2 mixture) has varied especially on positives, not negatives. These were occurred by transferring non-uniform concentrations of the 2nd Ab to the reaction zone. The irregular morphologies and locations of the dried 2nd Ab dispensed through manual pipetting resulted in the rehydration and transfer of the 2nd Ab being different in each test. The MOnITOR chip was designed to mainly conduct qualitative analysis on biomarkers, focusing on rapidly distinguishing positives and negatives by the threshold value. However, for the reliable detection, this problem should be analyzed and addressed. To address this problem, we are planning to adopt additional modules and automotive inkjet plotters to transfer rehydrated 2nd Ab at the same concentration in every test (Gökce et al., 2019).

4. Conclusion

. We developed the MOnITOR chip, a reliable one-step multiplex immunoassay with high-density self-assembled bead lines and a pixel intensity-based image analysis method, requiring minimal hands-on and turnaround time, similar to strip-based rapid tests. In principle, the MOnITOR chip can easily cover a broad spectrum of target immunoassays owing to its versatility. Depending on the embedded elements (i.e., antigens and antibodies on bead lines) and loaded samples from body fluids (e.g., serum, oropharyngeal, and nasopharyngeal swabs), various types of titer tests, such as those for screening immunity, plasma therapy, and vaccine candidates, could be performed (Hirotsu et al., 2020; Larremore et al., 2020; Theel et al., 2020). To potentially provide frequent and rapid in-field screening of large populations, a miniaturized benchtop fluorescence analyzer that can obtain snapshots of reacted bead lines and measure their final values can be integrated. An effective pixel extraction method will be embedded in the analyzer, thus enabling automatic, timely, and standardized diagnoses (Ballard et al., 2020). Importantly, the MOnITOR chip enables periodic and massive diagnosis, irrespective of patient symptoms. We anticipate that, after batch production and further studies, the MOnITOR platform will be a powerful clinical diagnostic tool.

CRediT authorship contribution statement

Wonhyung Lee: Conceptualization, Methodology, Investigation, Writing – original draft, Writing – review & editing, Validation, Formal analysis, Visualization. **Hojin Kim:** Conceptualization, Methodology, Writing – review & editing, Validation, Formal analysis. **Pan Kee Bae:** Conceptualization, Resources. **Sanghyun Lee:** Conceptualization, Methodology. **Sung Yang:** Funding acquisition, Resources. **Joonwon Kim:** Supervision.

Declaration of competing interest

The authors declare the following financial interests/personal relationships which may be considered as potential competing interests: Hojin Kim, Pan Kee Bae, Sanghyun Lee and Joonwon Kim are indicated as inventors in a patent (10–2061,191, Republic of Korea). All other authors declare no conflict of interest.

Acknowledgements

This research was supported by a grant from the Korea Health Technology R&D Project through the Korea Health Industry Development Institute (KHIDI), funded by the Ministry of Health and Welfare, Republic of Korea (Grant number: HI15C0001).

Appendix A. Supplementary data

Supplementary data to this article can be found online at https://doi.org/10.1016/j.bios.2021.113388.

References

Acharya, D., Bastola, P., Le, L., Paul, A.M., Fernandez, E., Diamond, M.S., Miao, W., Bai, F., 2016. An ultrasensitive electrogenerated chemiluminescence-based immunoassay for specific detection of Zika virus. Sci. Rep. 6, 32227.

Ballard, Z.S., Joung, H.A., Goncharov, A., Liang, J., Nugroho, K., Di Carlo, D., Garner, O. B., Ozcan, A., 2020. Deep learning-enabled point-of-care sensing using multiplexed paper-based sensors. NPJ Digit. Med. 3, 66.

Balmaseda, A., Stettler, K., Medialdea-Carrera, R., Collado, D., Jin, X., Zambrana, J.V., Jaconi, S., Cameroni, E., Saborio, S., Rovida, F., Percivalle, E., Ijaz, S., Dicks, S., Ushiro-Lumb, I., Barzon, L., Siqueira, P., Brown, D.W.G., Baldanti, F., Tedder, R., Zambon, M., de Filippis, A.M.B., Harris, E., Corti, D., 2017. Antibody-based assay discriminates Zika virus infection from other flaviviruses. Proc. Natl. Acad. Sci. U.S. A. 114 (31), 8384–8389.

Blicharz, T.M., Gong, P., Bunner, B.M., Chu, L.L., Leonard, K.M., Wakefield, J.A., Williams, R.E., Dadgar, M., Tagliabue, C.A., El Khaja, R., Marlin, S.L., Haghgooie, R., Davis, S.P., Chickering, D.E., Bernstein, H., 2018. Microneedle-based device for the one-step painless collection of capillary blood samples. Nat. Biomed. Eng. 2 (3), 151–157.

Brendish, N.J., Poole, S., Naidu, V.V., Mansbridge, C.T., Norton, N.J., Wheeler, H., Presland, L., Kidd, S., Cortes, N.J., Borca, F., Phan, H., Babbage, G., Visseaux, B., Ewings, S., Clark, T.W., 2020. Clinical impact of molecular point-of-care testing for suspected COVID-19 in hospital (COV-19POC): a prospective, interventional, non-randomised, controlled study. Lancet Respir. Med. 8 (12), 1192–1200.

Caruana, G., Croxatto, A., Coste, A.T., Opota, O., Lamoth, F., Jaton, K., Greub, G., 2020. Diagnostic strategies for SARS-CoV-2 infection and interpretation of microbiological results. Clin. Microbiol. Infect. 26 (9), 1178–1182.

Choi, S., Park, I., Hao, Z., Holman, H.Y., Pisano, A.P., Zohdi, T.I., 2010. Ultrafast self-assembly of microscale particles by open-channel flow. Langmuir 26 (7), 4661–4667.

Corman, V.M., Landt, O., Kaiser, M., Molenkamp, R., Meijer, A., Chu, D.K., Bleicker, T., Brunink, S., Schneider, J., Schmidt, M.L., Mulders, D.G., Haagmans, B.L., van der Veer, B., van den Brink, S., Wijsman, L., Goderski, G., Romette, J.L., Ellis, J., Zambon, M., Peiris, M., Goossens, H., Reusken, C., Koopmans, M.P., Drosten, C., 2020. Detection of 2019 novel coronavirus (2019-nCoV) by real-time RT-PCR. Euro Surveill. 25 (3).

Dimov, I.K., Basabe-Desmonts, L., Garcia-Cordero, J.L., Ross, B.M., Park, Y., Ricco, A.J., Lee, L.P., 2011. Stand-alone self-powered integrated microfluidic blood analysis system (SIMBAS). Lab Chip 11 (5), 845–850.

do Rosario, M.S., de Siqueira, I.C., 2020. Concerns about COVID-19 and arboviral (chikungunya, dengue, zika) concurrent outbreaks. Braz. J. Infect. Dis. 24 (6), 583–584.

Esbin, M.N., Whitney, O.N., Chong, S., Maurer, A., Darzacq, X., R, T., 2020. Overcoming the bottleneck to widespread testing: a rapid review of nucleic acid testing approaches for COVID-19 detection. RNA 26, 771–783.
FDA, 2021a. EUA Authorized Serology Test Performance. https://www.fda.gov/medical-devices/coronavirus-disease-2019-covid-19-emergency-use-authorizations-medical-devices/eua-authorized-serology-test-performance. (Accessed 13 April 2021).
FDA, 2021b. Individual EUAs for Antigen Diagnostic Tests for SARS-CoV-2. https://www.fda.gov/medical-devices/coronavirus-disease-2019-covid-19-emergency-use-authorizations-medical-devices/vitro-diagnostics-euas#individual-antigen. (Accessed 13 April 2021).
Gilboa, T., Maley, A.M., Ogata, A.F., Wu, C., Walt, D.R., 2021. Sequential protein capture in multiplex single molecule arrays: a strategy for eliminating assay cross-reactivity. Adv Healthc Mater 10 (4), e2001111.
Glière, A., Delattre, C., 2006. Modeling and fabrication of capillary stop valves for planar microfluidic systems. Sensor. Actuator. A 130–131, 601–608.
Gökce, O., Castonguay, S., Temiz, Y., Gervais, T., Delamarche, E., 2019. Self-coalescing flows in microfluidics for pulse-shaped delivery of reagents. Nature 574 (7777), 228–232.
Gubala, V., Harris, L.F., Ricco, A.J., Tan, M.X., Williams, D.E., 2012. Point of care diagnostics: status and future. Anal. Chem. 84 (2), 487–515.
Hatch, A.C., Fisher, J.S., Pentoney, S.L., Yang, D.L., Lee, A.P., 2011. Tunable 3D droplet self-assembly for ultra-high-density digital micro-reactor arrays. Lab Chip 11 (15), 2509–2517.
Hemmig, E., Temiz, Y., Gokce, O., Lovchik, R.D., Delamarche, E., 2020. Transposing lateral flow immunoassays to capillary-driven microfluidics using self-coalescence modules and capillary-assembled receptor carriers. Anal. Chem. 92 (1), 940–946.
Hirotsu, Y., Maejima, M., Shibusawa, M., Nagakubo, Y., Hosaka, K., Amemiya, K., Sueki, H., Hayakawa, M., Mochizuki, H., Tsutsui, T., Kakizaki, Y., Miyashita, Y., Yagi, S., Kojima, S., Omata, M., 2020. Comparison of automated SARS-CoV-2 antigen test for COVID-19 infection with quantitative RT-PCR using 313 nasopharyngeal swabs, including from seven serially followed patients. Int. J. Infect. Dis. 99, 397–402.
Ishige, T., Murata, S., Taniguchi, T., Miyabe, A., Kitamura, K., Kawasaki, K., Nishimura, M., Igari, H., Matsushita, K., 2020. Highly sensitive detection of SARS-CoV-2 RNA by multiplex rRT-PCR for molecular diagnosis of COVID-19 by clinical laboratories. Clin. Chim. Acta 507, 139–142.
Kim, D., Herr, A.E., 2013. Protein immobilization techniques for microfluidic assays. Biomicrofluidics 7 (4), 41501.
Kim, H., Chung, D.R., Kang, M., 2019. A new point-of-care test for the diagnosis of infectious diseases based on multiplex lateral flow immunoassays. Analyst 144 (8), 2460–2466.
Kim, H., Lee, S., Lee, W., Kim, J., 2017. High-density microfluidic particle-cluster-array device for parallel and dynamic study of interaction between engineered particles. Adv. Mater. 29 (31).
Kwak, T.J., Nam, Y.G., Najera, M.A., Lee, S.W., Strickler, J.R., Chang, W.J., 2016. Convex grooves in staggered herringbone mixer improve mixing efficiency of laminar flow in microchannel. PloS One 11 (11), e0166068.
Lai, C.C., Wang, C.Y., Ko, W.C., Hsueh, P.R., 2021. In vitro diagnostics of coronavirus disease 2019: technologies and application. J. Microbiol. Immunol. Infect. 54 (2), 164–174.
Larremore, D.B., Wilder, B., Lester, E., Shehata, S., Burke, J.M., Hay, J.A., Tambe, M., Mina, M.J., Parker, R., 2020. Test sensitivity is secondary to frequency and turnaround time for COVID-19 screening. Sci. Adv. eabd5393.
Lee, W., Kim, H., Lee, S., Kim, J., 2019. Continuous single-phase flow-assisted isolation for parallel observation of reactions between deterministically paired particles. J. Microelectromech. Syst. 28 (5), 882–889.
Lorenz, C., Azevedo, T.S., Chiaravalloti-Neto, F., 2020. COVID-19 and dengue fever: a dangerous combination for the health system in Brazil. Trav. Med. Infect. Dis. 35, 101659.
Mohd Hanafiah, K., Garcia, M., Anderson, D., 2013. Point-of-care testing and the control of infectious diseases. Biomarkers Med. 7 (3), 333–347.
Norman, M., Gilboa, T., Ogata, A.F., Maley, A.M., Cohen, L., Busch, E.L., Lazarovits, R., Mao, C.P., Cai, Y., Zhang, J., Feldman, J.E., Hauser, B.M., Caradonna, T.M., Chen, B., Schmidt, A.G., Alter, G., Charles, R.C., Ryan, E.T., Walt, D.R., 2020. Ultrasensitive high-resolution profiling of early seroconversion in patients with COVID-19. Nat Biomed Eng 4 (12), 1180–1187.
Olanrewaju, A., Beaugrand, M., Yafia, M., Juncker, D., 2018. Capillary microfluidics in microchannels: from microfluidic networks to capillaric circuits. Lab Chip 18 (16), 2323–2347.
Oran, D.P., Topol, E.J., 2020. Prevalence of asymptomatic SARS-CoV-2 infection : a narrative review. Ann. Intern. Med. 173 (5), 362–367.
Quick, J., Loman, N.J., Duraffour, S., Simpson, J.T., Severi, E., Cowley, L., Bore, J.A., Koundouno, R., Dudas, G., Mikhail, A., Ouedraogo, N., Afrough, B., Bah, A., Baum, J. H., Becker-Ziaja, B., Boettcher, J.P., Cabeza-Cabrerizo, M., Camino-Sanchez, A., Carter, L.L., Doerrbecker, J., Enkirch, T., Dorival, I.G.G., Hetzelt, N., Hinzmann, J., Holm, T., Kafetzopoulou, L.E., Koropogui, M., Kosgey, A., Kuisma, E., Logue, C.H., Mazzarelli, A., Meisel, S., Mertens, M., Michel, J., Ngabo, D., Nitzsche, K., Pallash, E., Patrono, L.V., Portmann, J., Repits, J.G., Rickett, N.Y., Sachse, A., Singethan, K., Vitoriano, I., Yemanaberhan, R.L., Zekeng, E.G., Trina, R., Bello, A., Sall, A.A., Faye, O., Faye, O., Magassouba, N., Williams, C.V., Amburgey, V., Winona, L., Davis, E., Gerlach, J., Washington, F., Monteil, V., Jourdain, M., Bererd, M., Camara, A., Somlare, H., Camara, A., Gerard, M., Bado, G., Baillet, B., Delaune, D., Nebie, K.Y., Diarra, A., Savane, Y., Pallawo, R.B., Gutierrez, G.J., Milhano, N., Roger, I., Williams, C.J., Yattara, F., Lewandowski, K., Taylor, J., Rachwal, P., Turner, D., Pollakis, G., Hiscox, J.A., Matthews, D.A., O'Shea, M.K., Johnston, A.M., Wilson, D., Hutley, E., Smit, E., Di Caro, A., Woelfel, R., Stoecker, K., Fleischmann, E., Gabriel, M., Weller, S.A., Koivogui, L., Diallo, B., Keita, S., Rambaut, A., Formenty, P., Gunther, S., Carroll, M.W., 2016. Real-time, portable genome sequencing for Ebola surveillance. Nature 530 (7589), 228–232.
Ryu, W., Huang, Z., Sun Park, J., Moseley, J., Grossman, A.R., Fasching, R.J., Prinz, F.B., 2008. Open micro-fluidic system for atomic force microscopy-guided in situ electrochemical probing of a single cell. Lab Chip 8 (9), 1460–1467.
Sankova, N., Shalaev, P., Semeykina, V., Dolgushin, S., Odintsova, E., Parkhomchuk, E., 2020. Spectrally encoded microspheres for immunofluorescence analysis. J. Appl. Polym. Sci. 138 (8).
Shrivastava, S., Trung, T.Q., Lee, N.E., 2020. Recent progress, challenges, and prospects of fully integrated mobile and wearable point-of-care testing systems for self-testing. Chem. Soc. Rev. 49 (6), 1812–1866.
Smyrlaki, I., Ekman, M., Lentini, A., Rufino de Sousa, N., Papanicolaou, N., Vondracek, M., Aarum, J., Safari, H., Muradrasoli, S., Rothfuchs, A.G., Albert, J., Hogberg, B., Reinius, B., 2020. Massive and rapid COVID-19 testing is feasible by extraction-free SARS-CoV-2 RT-PCR. Nat. Commun. 11 (1), 4812.
Theel, E.S., Slev, P., Wheeler, S., Couturier, M.R., Wong, S.J., Kadkhoda, K., 2020. The role of antibody testing for SARS-CoV-2: is there one? J. Clin. Microbiol. 58 (8).
van Doremalen, N., Bushmaker, T., Morris, D.H., Holbrook, M.G., Gamble, A., Williamson, B.N., Tamin, A., Harcourt, J.L., Thornburg, N.J., Gerber, S.I., Lloyd-Smith, J.O., de Wit, E., Munster, V.J., 2020. Aerosol and surface stability of SARS-CoV-2 as compared with SARS-CoV-1. N. Engl. J. Med. 382 (16), 1564–1567.
Verduyn, M., Allou, N., Gazaille, V., Andre, M., Desroche, T., Jaffar, M.C., Traversier, N., Levin, C., Lagrange-Xelot, M., Moiton, M.P., Hoang, S., 2020. Co-infection of dengue and COVID-19: a case report. PLoS Neglected Trop. Dis. 14 (8), e0008476.
Wang, Y.C., Lee, Y.T., Yang, T., Sun, J.R., Shen, C.F., Cheng, C.M., 2020. Current diagnostic tools for coronaviruses-From laboratory diagnosis to POC diagnosis for COVID-19. Bioeng. Transl. Med., e10177
West, J.S., Perryman, S.A.M., 2020. COVID-19: dogma over potential for prolonged droplet dispersal in air. Front. Public Health 8, 551836.
Whitman, J.D., Hiatt, J., Mowery, C.T., Shy, B.R., Yu, R., Yamamoto, T.N., Rathore, U., Goldgof, G.M., Whitty, C., Woo, J.M., Gallman, A.E., Miller, T.E., Levine, A.G., Nguyen, D.N., Bapat, S.P., Balcerek, J., Bylsma, S.A., Lyons, A.M., Li, S., Wong, A.W., Gillis-Buck, E.M., Steinhart, Z.B., Lee, Y., Apathy, R., Lipke, M.J., Smith, J.A., Zheng, T., Boothby, I.C., Isaza, E., Chan, J., Acenas 2nd, D.D., Lee, J., Macrae, T.A., Kyaw, T.S., Wu, D., Ng, D.L., Gu, W., York, V.A., Eskandarian, H.A., Callaway, P.C., Warrier, L., Moreno, M.E., Levan, J., Torres, L., Farrington, L.A., Loudermilk, R.P., Koshal, K., Zorn, K.C., Garcia-Beltran, W.F., Yang, D., Astudillo, M.G., Bernstein, B. E., Gelfand, J.A., Ryan, E.T., Charles, R.C., Iafrate, A.J., Lennerz, J.K., Miller, S., Chiu, C.Y., Stramer, S.L., Wilson, M.R., Manglik, A., Ye, C.J., Krogan, N.J., Anderson, M.S., Cyster, J.G., Ernst, J.D., Wu, A.H.B., Lynch, K.L., Bern, C., Hsu, P.D., Marson, A., 2020. Evaluation of SARS-CoV-2 serology assays reveals a range of test performance. Nat. Biotechnol. 38 (10), 1174–1183.
WHO, 2016. Target Product Profiles for Better Diagnostic Tests for Zika Virus Infection.
WHO, 2021. COVID-19 Pandemic. https://www.who.int/emergencies/diseases/novel-coronavirus-2019. (Accessed 13 April 2021).
Xia, Y., Whitesides, G.M., 1998. Soft lithography. Angew. Chem. 37, 550–575.
Yan, G., Lee, C.K., Lam, L.T.M., Yan, B., Chua, Y.X., Lim, A.Y.N., Phang, K.F., Kew, G.S., Teng, H., Ngai, C.H., Lin, L., Foo, R.M., Pada, S., Ng, L.C., Tambyah, P.A., 2020. Covert COVID-19 and false-positive dengue serology in Singapore. Lancet Infect. Dis. 20 (5).
Yeh, E.C., Fu, C.C., Hu, L., Thakur, R., Feng, J., Lee, L.P., 2017. Self-powered integrated microfluidic point-of-care low-cost enabling (SIMPLE) chip. Sci Adv 3 (3), e1501645.
Zhao, J., Yuan, Q., Wang, H., Liu, W., Liao, X., Su, Y., Wang, X., Yuan, J., Li, T., Li, J., Qian, S., Hong, C., Wang, F., Liu, Y., Wang, Z., He, Q., Li, Z., He, B., Zhang, T., Fu, Y., Ge, S., Liu, L., Zhang, J., Xia, N., Zhang, Z., 2020. Antibody responses to SARS-CoV-2 in patients of novel coronavirus disease 2019. Clin. Infect. Dis. 71 (16), 2027–2034.